



Article (refereed) – Published version

Polton, Jeff A.; Lenn, Yueng-Djern; Elipot, Shane; Chereskin, Teresa K.; Sprintall, Janet. 2013 Can Drake Passage Observations Match Ekman's Classic Theory? *Journal of Physical Oceanography*, 43 (8). 1733-1740. [10.1175/JPO-D-13-034.1](https://doi.org/10.1175/JPO-D-13-034.1)

This version available at <http://nora.nerc.ac.uk/503111/>

NERC has developed NORA to enable users to access research outputs wholly or partially funded by NERC. Copyright and other rights for material on this site are retained by the rights owners. Users should read the terms and conditions of use of this material at

<http://nora.nerc.ac.uk/policies.html#access>

© Copyright 2013 American Meteorological Society (AMS).
Permission to use figures, tables, and brief excerpts from this work in scientific and educational works is hereby granted provided that the source is acknowledged. Any use of material in this work that is determined to be “fair use” under Section 107 of the U.S. Copyright Act September 2010 Page 2 or that satisfies the conditions specified in Section 108 of the U.S. Copyright Act (17 USC §108, as revised by P.L. 94-553) does not require the AMS’s permission. Republication, systematic reproduction, posting in electronic form, such as on a web site or in a searchable database, or other uses of this material, except as exempted by the above statement, requires written permission or a license from the AMS. Additional details are provided in the AMS Copyright Policy, available on the AMS Web site located at (<http://www.ametsoc.org/>) or from the AMS at 617-227-2425 or copyrights@ametsoc.org.

Contact NOC NORA team at
publications@noc.soton.ac.uk

Can Drake Passage Observations Match Ekman's Classic Theory?

JEFF A. POLTON

National Oceanography Centre, Liverpool, United Kingdom

YUENG-DJERN LENN

School of Ocean Sciences, Bangor University, Menai Bridge, United Kingdom

SHANE ELIPOT

Rosenstiel School of Marine and Atmospheric Science, University of Miami, Miami, Florida

TERESA K. CHERESKIN AND JANET SPRINTALL

Scripps Institution of Oceanography, University of California, San Diego, La Jolla, California

(Manuscript received 12 February 2013, in final form 11 April 2013)

ABSTRACT

Ekman's theory of the wind-driven ocean surface boundary layer assumes a constant eddy viscosity and predicts that the current rotates with depth at the same rate as it decays in amplitude. Despite its wide acceptance, Ekman current spirals are difficult to observe. This is primarily because the spirals are small signals that are easily masked by ocean variability and cannot readily be separated from the geostrophic component. This study presents a method for estimating ageostrophic currents from shipboard acoustic Doppler current profiler data in Drake Passage and finds that observations are consistent with Ekman's theory. By taking into account the sampling distributions of wind stress and ageostrophic velocity, the authors find eddy viscosity values in the range of 0.08–0.12 m² s⁻¹ that reconcile observations with the classic theory in Drake Passage. The eddy viscosity value that most frequently reconciles observations with the classic theory is 0.094 m² s⁻¹, corresponding to an Ekman depth scale of 39 m.

1. Introduction

The Ekman (1905) paper describes the nature of steady spiraling velocity profiles in boundary layers, by assuming a stress parameterization that is a linear function of shear. In this model, the vertical shear stress is balanced by the Coriolis force resulting in the now familiar Ekman spirals that, in the upper ocean, decay in magnitude as they rotate with depth. The constant of proportionality between the stress and shear is the turbulent eddy viscosity κ . If we write the horizontal velocity as a complex quantity with real and imaginary parts in the eastward and northward directions,

respectively, then the Ekman velocity $\mathbf{u}^E(z)$ as a function of depth z , in the Southern Hemisphere, is given by

$$\mathbf{u}^E(z) = \frac{\sqrt{2}\boldsymbol{\tau}_0}{D|f|\rho_0} e^{-z/D} e^{i(\pi/4 - z/D)}, \quad \text{where } D = \sqrt{\frac{2\kappa}{|f|}} \quad (1)$$

is the Ekman depth scale, z increases upward and is zero at the surface, $|f|$ is the magnitude of the Coriolis parameter, $i = \sqrt{-1}$, and $\boldsymbol{\tau}_0$ is the wind stress vector also written as a complex quantity. Therefore, for real and constant κ , this Ekman model predicts the same constant exponential decay scale D for the magnitude and the rotation of the velocity vector.

On the rare occasions where Ekman spirals have been observed in the open ocean (e.g., Price et al. 1987; Wijffels et al. 1994; Chereskin 1995; Lenn and Chereskin 2009; Elipot and Gille 2009), the spirals are typically “flatter” than theoretical spirals: the rate of vector amplitude decay exceeds the rate of vector rotation with depth.

 Denotes Open Access content.

Corresponding author address: J. Polton, NOC, 6 Brownlow Street, Liverpool L3 5DA, United Kingdom.
E-mail: jelt@noc.ac.uk

DOI: 10.1175/JPO-D-13-034.1

Lenn and Chereskin (2009, hereafter LC09) analyzed oceanic velocity from transects of Drake Passage using underway acoustic Doppler current profiler (ADCP) data. They extracted the upper-ocean ageostrophic velocity profile from this dataset by removing an estimate of the geostrophic velocity, assumed constant with depth, taken as the ADCP velocity at 98 m. This method was based on a favorable comparison, at that depth, between the vertical shear of the ADCP cross-track velocities and independent geostrophic cross-track velocity shear estimated from expendable bathythermograph (XBT) and expendable conductivity–temperature–depth (XCTD) observations that were made on about a third of the transects (Sprintall 2003). The mean of such ageostrophic currents shows a typical flattened Ekman spiral. Here, we analyze the observations of LC09 again to show that if a geostrophic velocity with constant shear (Chereskin and Roemmich 1991; Wijffels et al. 1994), rather than constant geostrophic velocity, is subtracted from the ADCP velocity then the resulting average Ekman spiral is actually not flattened. Moreover, an eddy viscosity can be fitted to a real number consistent with (1) if the uncertainties in observations are duly accounted for.

2. The Drake Passage datasets

Underway velocity data were collected by the Antarctic Research and Supply Vessel (ARSV) *Laurence M. Gould* (LMG) using an ADCP transducer, which measures currents in the upper 250 m. The ADCP instrument was configured such that the shallowest depth bins are centered at 22 or 26 m and spaced 8 m apart. Here, we update the data used in LC09 from 156 (September 1999–October 2006) to 242 crossings (up to April 2011) of Drake Passage (Fig. 1). A full description of the data collection and processing is provided in LC09 and Firing et al. (2012).

Repeat XBT and XCTD surveys of Drake Passage are conducted roughly six times yearly by the LMG (Sprintall 2003). This study uses 59 XBT/XCTD surveys of upper-ocean temperature coincident with ADCP velocities between September 1999 and April 2011. Salinities were inferred from climatologically based salinity–temperature–depth regressions and then corrected by XCTD salinity anomalies where available. The XBT temperatures and salinities are then objectively mapped to a grid of 0.1° latitude and 10-m depth from which the cross-track component of geostrophic velocity, referenced to zero at 800 m, is obtained (Sprintall 2003).

We use the cross-calibrated multi-platform (CCMP) 10-m winds at 0.25° and 6-hourly resolution (Atlas et al. 2011) from 2000 to 2010, overlapping the LMG dataset during 120 of 127 months. We compute wind stress from

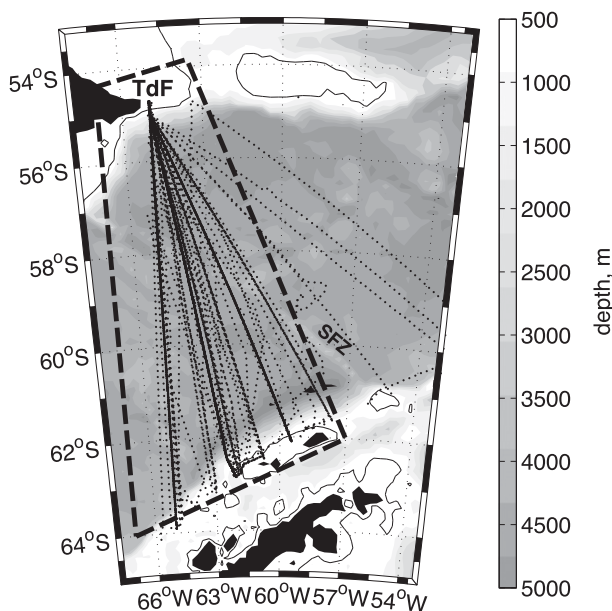


FIG. 1. Map of Drake Passage with bathymetry (Smith and Sandwell 1997) shaded in gray scale and LMG cruise tracks overlaid (dotted lines). Mean Ekman currents and wind stresses are computed from observations within the region bounded by the thick dashed line. Geographic locations of Tierra del Fuego (TdF) and the Shackleton Fracture Zone (SFZ) are marked.

10-m winds using drag coefficients from Yelland and Taylor (1996) for wind speeds in the range from 3 to 26 m s^{-1} . For wind speeds outside of this range, we assume constant drag coefficients set to the minimum or maximum values determined from Yelland and Taylor (1996), as in Gille (2005). To match the region covered by ADCP observations, we have only included wind data points within the dashed line in Fig. 1. The mean wind stress vector and standard error ellipse are shown in Fig. 5 (described in greater detail below).

3. Extracting the Ekman velocities

In the analysis by LC09 of the 1999–2006 ADCP and XBT/XCTD dataset, the geostrophic component of the cross-track shear was shown to be significantly smaller than the ageostrophic component above ~ 100 -m depth. Hence, following previous studies (Price et al. 1987; Chereskin 1995; Elipot and Gille 2009), for each profile, they subtracted the observed ADCP current at 98 m from the current depth bins above to infer profiles of ageostrophic current. However, inspection of the XBT/XCTD velocities (Fig. 2a) shows a depth-varying cross-track structure. Following Chereskin and Roemmich (1991) and Wijffels et al. (1994), a sheared geostrophic velocity is instead removed from the ADCP data to compute the ageostrophic profile.

Section-by-section comparisons of the ADCP- and XBT/XCTD-inferred velocities show that while the

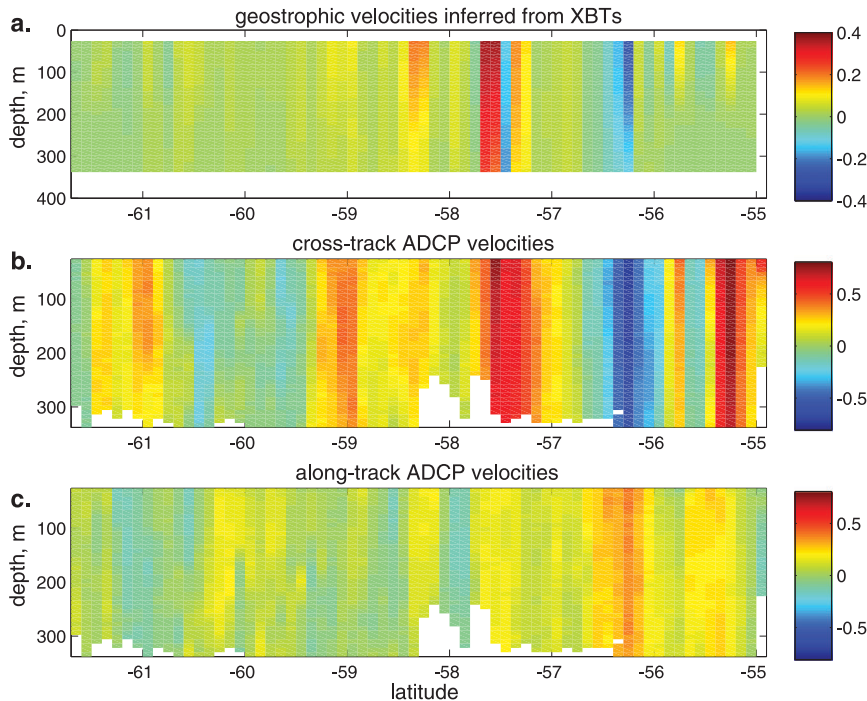


FIG. 2. Comparison of Drake Passage velocity data (m s^{-1}) from a typical (November 2000) transect. (a) Cross-track XBT-inferred geostrophic velocity. (b) Cross-track ADCP direct velocity. (c) Along-track ADCP direct velocity.

geostrophic component dominates the cross-track velocity, the along-track ADCP velocity is frequently of similar magnitude and should be accounted for in the total geostrophic current and shear (Fig. 2). Because the XBT/XCTD data cannot provide the along-track component of the geostrophic shear, we devise a method to estimate the total geostrophic shear from the ADCP data only.

First, the geostrophic shear is estimated from the ADCP velocity shear at depths (≥ 150 m) well below the Ekman layer (~ 98 m in LC09). Below 150 m, both the XBT/XCTD and ADCP current profiles are dominated by a weakly sheared vertically coherent flow (Lenn et al. 2007), but direct comparisons show that the cross-track component of the ADCP-inferred deep shear has a much greater variance than the XBT-inferred shear (Fig. 3a) because of nonpressure-driven currents (e.g., internal waves) in the ADCP measurements. As such, the deep ADCP shear is best obtained from the slope of a linear fit to the ADCP currents between 150 m and the signal depth maximum (~ 300 m). The resulting overall cross-track mean shears below 150 m are in close agreement on average (Fig. 3b). There are, however, significant regional differences in the mean geostrophic shear (Firing et al. 2011). We take this into account by sorting the ADCP currents into 25 km by 25 km grid boxes and computing mean geostrophic shear from the mean current profile in each grid box.

Second, an instantaneous geostrophic current profile is obtained by extrapolating the instantaneous 150-m ADCP current upward to the shallowest bin, assuming the mean constant geostrophic shear for that grid box. These regionally varying instantaneous geostrophic profiles are then subtracted from each instantaneous ADCP current profile to obtain residual ageostrophic currents. These are averaged within each grid box and then over the whole Drake Passage LMG domain to produce a new mean estimate of ageostrophic currents with associated standard error ellipses (Fig. 4). A limitation of this method is that it increases the variance in the estimate of geostrophic velocities subtracted from the total currents, and consequently, increases the standard error in the mean ageostrophic current profile. However, we find that this increase in variance is compensated by extending the time series, compared to LC09. A marked advantage of this method is that it is not dependent on setting a depth at which ageostrophic velocities vanish, except for the reasonable assumption that it is shallower than 150 m.

4. Validating the constant eddy viscosity Ekman model

The resulting ageostrophic current profile (Fig. 4b) clearly shows a spiral that rotates anticlockwise with

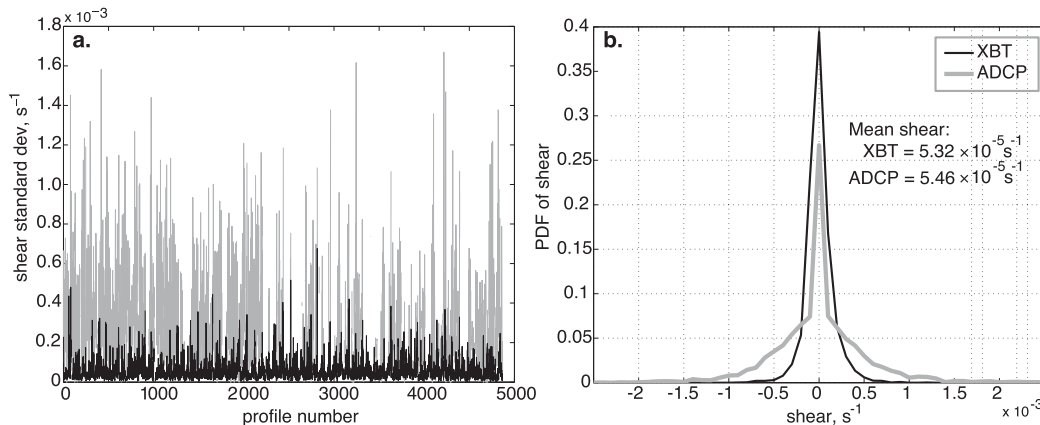


FIG. 3. (a) Comparison of the std dev in the mean cross-track shear below 150 m computed from the XBT geostrophic currents (black) and the ADCP currents (gray) for all the collocated profiles from September 1999 to April 2011. (b) Probability density functions (PDF) of the mean shear below 150 m taken directly from the XBT geostrophic currents (black) and deduced from a linear fit to the ADCP currents (gray) for all the collocated profiles from September 1999 to April 2011.

depth as the magnitude diminishes, in qualitative agreement with Ekman's theory. The log magnitude and current phase (relative to the most shallow data point) vary linearly with depth (Fig. 4a). Also shown (smaller symbols with dashed lines) are the depth-varying phase and log magnitude relationships when a constant geostrophic velocity is removed from the direct ADCP velocities (as in LC09) instead of a constant geostrophic shear. Clearly, accounting for the geostrophic shear (and without including any wave effects) removes the Ekman spiral 'flattening' effect.

We use the uncertainty of the current estimates (as represented by the standard error ellipses in Fig. 4b) to assess whether the constant and real eddy viscosity hypothesis should be rejected, and therefore whether these data are consistent with model (1). Given a wind stress vector $\boldsymbol{\tau}_0$, Ekman's model (1) predicts the velocity profile for which κ is a free parameter. We estimate κ as the value that minimizes the error ϵ between observed and predicted profiles, where ϵ is the largest absolute difference between the profiles. Additionally, we enforce the consistency criterion that this maximum error lies within the standard error ellipse of the velocity vector at the corresponding depth. Algebraically,

$$\epsilon = \begin{cases} G & \text{for } G < 1 \\ \infty & \text{for } G \geq 1 \end{cases}; \quad \boldsymbol{\delta}(z) = [\mathbf{u}^{\text{obs}}(z) - \mathbf{u}(z)]e^{-i\phi(z)};$$

$$G = \max_z \left(\left\{ \frac{\text{Re}[\boldsymbol{\delta}(z)]}{u_M(z)} \right\}^2 + \left\{ \frac{\text{Im}[\boldsymbol{\delta}(z)]}{u_m(z)} \right\}^2 \right),$$

where $\boldsymbol{\delta}(z)$ is a two-dimensional measure of the difference between the predicted $\mathbf{u}(z)$ and observed $\mathbf{u}^{\text{obs}}(z)$

velocity profiles that has been counter rotated by the orientation (with respect to the east) of the observational error ellipse $\phi(z)$. Scalar error score G occurs where the components of $\boldsymbol{\delta}(z)$ are normalized by the major $u_M(z)$ and minor $u_m(z)$ standard error ellipse axes. Because $\mathbf{u}(z)$ is a function of κ and $\boldsymbol{\tau}_0$, the error score ϵ is also a function of κ and $\boldsymbol{\tau}_0$.

Figure 5 shows contours of optimum κ values as a function of all wind stress $\boldsymbol{\tau}_0$ defined by the mean and the standard error ellipse of the wind stress over the Drake Passage area. The inset panel of the same figure shows contours, also as a function of $\boldsymbol{\tau}_0$, of the range of the κ parameter satisfying the consistency criterion. It is apparent that not all values of wind stress, within one standard error of the mean, can be reconciled with the observed velocities using (1). The wind stresses in the distribution can be approximately split into two categories. Those with an eastward component that is smaller than the mean are not consistent with the constant eddy viscosity model, whereas the wind stresses with an eastward component that is larger than the mean have an increasing range of κ that are consistent with the observations. The hodographs for all consistent Ekman solutions are bound by the gray envelope in Fig. 4b. At first glance, the spread appears narrow. The width of the envelope is controlled by the range of κ and the vector range of $\boldsymbol{\tau}_0$, because the surface Ekman current is given by $e^{i\pi/4}\boldsymbol{\tau}_0/(\rho_0\sqrt{\kappa|f|})$ and the curvature of the hodograph increases as κ decreases. However, the curvature is bound by the standard error ellipses at the second ($z = -34$ m) and sixth ($z = -66$ m) depth bins (shown with dashed ellipses in Fig. 4b) and $\boldsymbol{\tau}_0$ has a relatively small variance (Fig. 5 inset shows the relative sizes of the magnitude

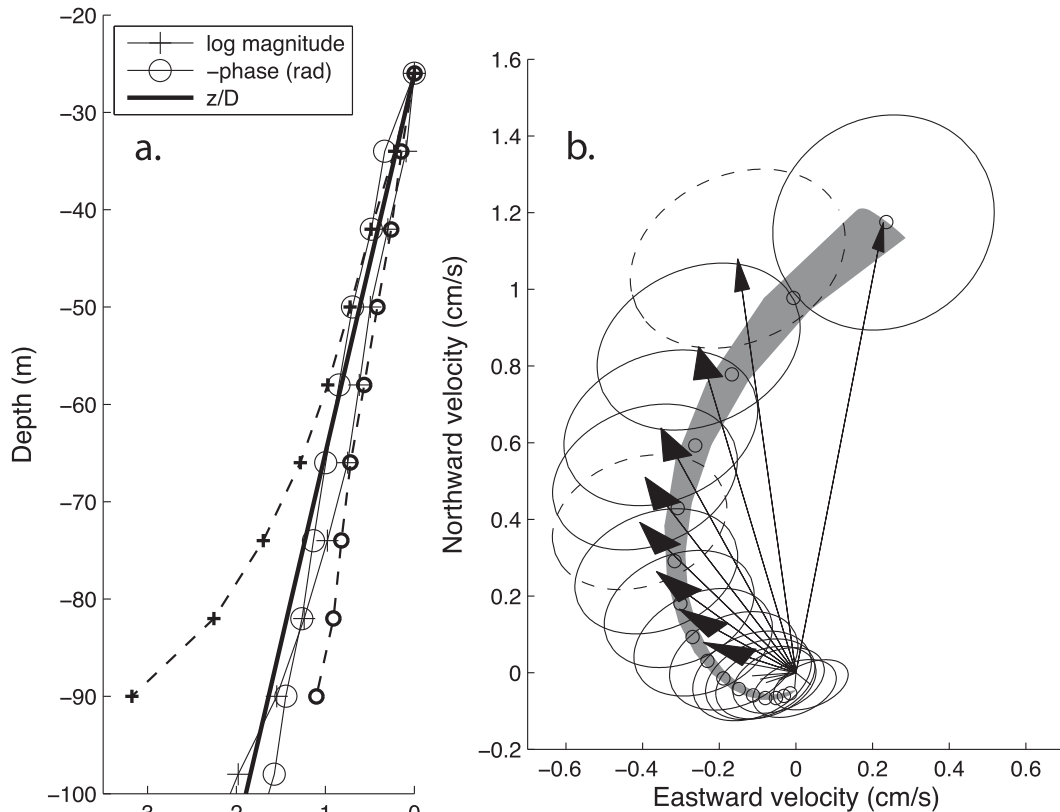


FIG. 4. Eddy viscosity values can be found that are consistent with the constant eddy viscosity Ekman model. (a) Decay scales for the log magnitude and negative phase of the ageostrophic profile relative to the shallowest value preceding (small gray symbols on dashed lines) and proceeding (large symbols on solid lines) removal of geostrophic shear. The thick black line shows the decay scale, common to both the magnitude and phase, for the value of $\kappa = \hat{\kappa}$, that most frequently reconciles observations with the model. To overlay magnitude and phase data, the negative phase is shown increasing clockwise. (b) Hodograph and std error ellipses for the ageostrophic profile are shown. The gray envelope bounds the set of hodographs where the model is consistent with observations. By construction, these fall within the observed error ellipses. Circle markers show the Ekman solution at observation data depths for $\kappa = \hat{\kappa}$. Arrow heads are only shown for $z \geq -90$ m. The dashed ellipses show the depths at which the envelope is bound by the std error ellipses: at -34 m (second depth bin) the envelope is bound to the southeast and at -66 m the envelope is bound to the southwest.

and standard error ellipse of the wind stress). Combined, these result in a narrow envelope.

The range of eddy viscosity values, across all permitted wind stresses, is relatively narrow: $0.084 < \kappa < 0.118 \text{ m}^2 \text{ s}^{-1}$, especially when compared to previous estimates when the spiral appears flattened ($0.03 < \kappa < 0.22 \text{ m}^2 \text{ s}^{-1}$; LC09). Assuming a uniform distribution for all τ_0 bound by the standard error ellipse of the wind stress, a PDF of eddy viscosity coefficients that satisfy the consistency criterion is computed (Fig. 6). The resulting PDF has an asymmetric spread and a mode at $\hat{\kappa} = 0.094 \text{ m}^2 \text{ s}^{-1}$. The Ekman solution with $\kappa = \hat{\kappa}$ and τ_0 chosen to best fit the observations is shown as a black line in Fig. 4a and plotted as circles at the same depth as the observations in Fig. 4b. This corresponds to an Ekman depth scale $D = 39$ m.

5. Discussion

We have shown that, accounting for the geostrophic shear neglected in LC09, observations in Drake Passage can be consistent with the classic Ekman theory (with constant eddy viscosity). This result stands in contrast to previous studies (Wijffels et al. 1994; Chereskin 1995; Price and Sundermeyer 1999; Lenn and Chereskin 2009) that report flattened Ekman spirals, where the decay rate of magnitude and turning do not match. Here, a range of eddy viscosity values were found that can reconcile the observational ageostrophic velocity profiles to Ekman theory.

This flattening has been variously reported to be consistent with diurnal cycling of stratification (Price and Sundermeyer 1999), surface gravity wave Stokes–Coriolis

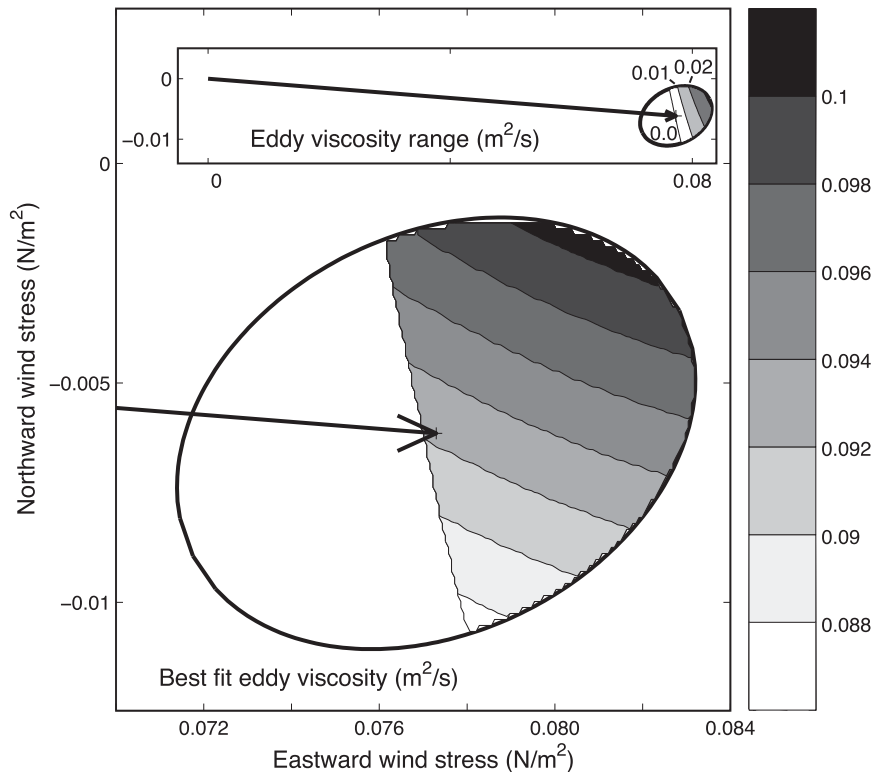


FIG. 5. Eddy viscosity diagnostics projected into the 10-m CCMP wind stress (arrow) error ellipse. The shading denotes κ for the Ekman spiral that best fits the observational values and (in the inset panel, plotted on the same axes) the range of κ that reconciles Ekman's balance with the observations. For wind stress values in the noncontoured portion of the error ellipse, all Ekman solutions (with free parameter κ) are at least one std error from the observations for at least one observational depth level.

forcing (Polton et al. 2005), eastward velocity displacement (Heinloo and Toompuu 2012), more complex eddy viscosity profiles (Madsen 1977; Lewis and Belcher 2004; Zikanov et al. 2003; Polton et al. 2005; McWilliams and Huckle 2006; McWilliams et al. 2012), or frequency-dependent effects (Elipot and Gille 2009). However, we demonstrate that the associated increase in complexity is not necessarily justified given the (quantified) uncertainty in these data. In Drake Passage, the effects of geostrophic shear are sufficient to reconcile the observations to the classic theory. Plotting the ageostrophic profiles of log magnitude and phase (Fig. 4a); it is clear that there is a significant collapse of the magnitude and phase data toward a common depth scale. This suggests that a constant eddy viscosity model will suffice.

It does seem likely though, of all the places in the global oceans, that Drake Passage would be ideal to see the effects of surface gravity waves. The Lagrangian transport \mathbf{T}_s associated with Stokes drift in Drake Passage is approximately $0.5 \text{ m}^2 \text{ s}^{-1}$, eastward (McWilliams and Restrepo 1999). This is several times larger than the wind-driven transport ($0.08 \text{ m}^2 \text{ s}^{-1}$, northward). In the

presence of surface gravity waves, the depth-integrated momentum balance is modified to include Lagrangian transport (e.g., Polton et al. 2005),

$$\int_{-\infty}^0 \mathbf{u}^E(z) dz = -i \frac{\boldsymbol{\tau}_0}{\rho_0 f} - \mathbf{T}_s.$$

Therefore, if Stokes drift is important in Drake Passage, the velocity profile (that fits observed Eulerian data and is integrated to the surface) must be significantly modified to accommodate the additional \mathbf{T}_s in this momentum balance. This can only happen above the shallowest bin. With the estimated Ekman depth scale of 39 m, 49% of the transport occurs above this first bin. There is, therefore, scope to include a mixed layer slab model to the ageostrophic profile that would result in the depth-integrated Eulerian transport falling westward of the wind-driven target. The discrepancy would be consistent with the direction of the Lagrangian Stokes transport. Unfortunately, we do not have robust estimates of the Stokes drift (Webb and Fox-Kemper 2011), and though it can be fitted, it is also a function of the

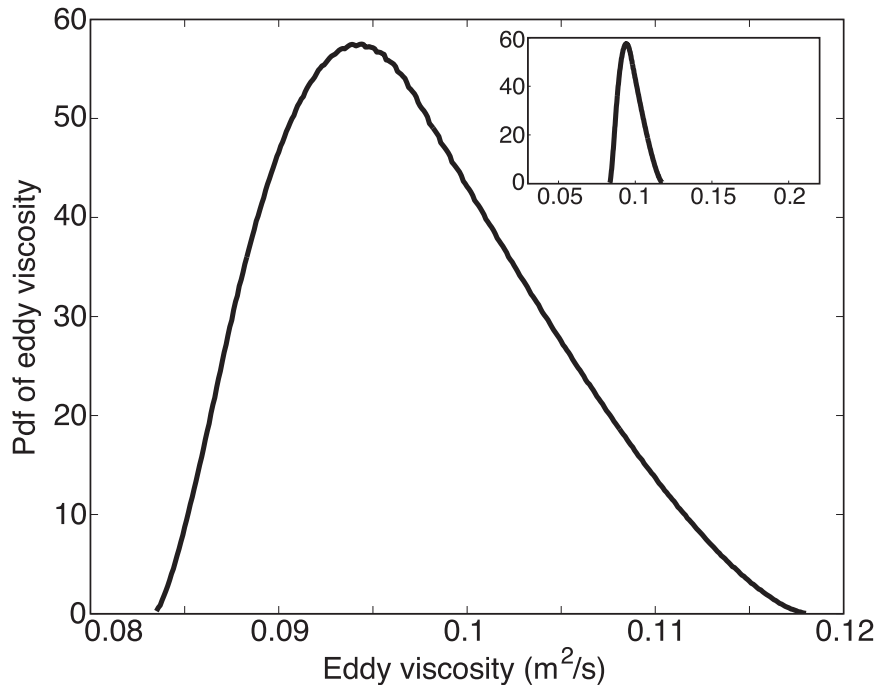


FIG. 6. PDF of eddy viscosity κ deduced from ADCP observations assuming a constant eddy viscosity model and a known wind stress. The spread of values is deduced by seeking possible solutions where the mean wind stress and ageostrophic velocity measurements are allowed to vary by one std error. The mode value represents the most likely value of $\kappa = 0.094 \text{ m}^2 \text{ s}^{-1}$. The mean, median, and interquartile range are 0.097, 0.096, and $0.010 \text{ m}^2 \text{ s}^{-1}$. The inset panel shows the PDF plotted on the viscosity range presented in LC09.

unknown mixed layer depth. This is beyond the scope of the intended study.

In this study, we have presented “uncertainty” in terms of the standard error ellipses. It has not been possible to quantify the actual errors in the ageostrophic velocity as the difference of the total and geostrophic flow. These errors may be considerable. Rudnick (2003) and McWilliams and Huckle (2006) also suggest that the steady-state assumption in the basic Ekman theory is too simplistic for the real ocean. While this is certainly a valid concern, cancelation between multiple higher-complexity processes is necessary to achieve results of the same consistency as the constant eddy viscosity model. Though more complete physics is desirable from a pedagogical stand point, our analysis of these data suggests that there is insufficient evidence to discard the constant eddy viscosity model in favor of a more complex physical system.

Acknowledgments. Dr. Jeff Polton receives support from a NERC New Investigator Grant (NE/I002103/1) and Dr. Yueng-Djern Lenn is supported by a NERC UK Postdoctoral Fellowship. We also acknowledge support from the National Science Foundation Office of Polar Programs, ANT-9816226/-0338103/-0838750/-0838714

(ADCP), and ANT-0003618/0337998/0943818 (XBT). We are also grateful to the captain and crew of the ARSV *Laurence M. Gould* and to Raytheon Polar Services Corporation for their excellent technical and logistical support on the cruises. Eric Firing, Jules Hummon, and Sharon Escher have been invaluable for their contribution to the ADCP data collection, processing, and editing. Many thanks to Sarah Gille and Magdalena Carranza on the appropriate choice of wind product.

REFERENCES

- Atlas, R., R. N. Hoffman, J. Ardizzone, S. M. Leidner, J. C. Jusem, D. K. Smith, and D. Gombos, 2011: A cross-calibrated, multiplatform ocean surface wind velocity product for meteorological and oceanographic applications. *Bull. Amer. Meteor. Soc.*, **92**, 157–174.
- Chereskin, T. K., 1995: Direct evidence for an Ekman balance in the California Current. *J. Geophys. Res.*, **100** (C9), 18261–18269.
- , and D. Roemmich, 1991: A comparison of measured and wind-derived Ekman transport at 11°N in the Atlantic Ocean. *J. Phys. Oceanogr.*, **21**, 869–878.
- Ekman, V. W., 1905: On the influence of the Earth’s rotation on ocean-currents. *Ark. Mat. Astron. Fys.*, **2**, 1–52.

- Elipot, S., and S. T. Gille, 2009: Ekman layers in the Southern Ocean: Spectral models and observations, vertical viscosity and boundary layer depth. *Ocean Sci.*, **5**, 115–139.
- Firing, E., J. Hummon, and T. Chereskin, 2012: Improving the quality and accessibility of current profile measurements in the Southern Ocean. *Oceanography*, **25**, 164–165, doi:10.5670/oceanog.2012.91.
- Firing, Y. L., T. K. Chereskin, and M. R. Mazloff, 2011: Vertical structure and transport of the Antarctic Circumpolar Current in Drake Passage from direct velocity observations. *J. Geophys. Res.*, **116**, C08015, doi:10.1029/2011JC006999.
- Gille, S. T., 2005: Statistical characterization of zonal and meridional wind stress. *J. Atmos. Oceanic Technol.*, **22**, 1353–1372.
- Heinloo, J., and A. Toompuu, 2012: A modification of the classical Ekman model accounting for the Stokes drift and stratification effects. *Environ. Fluid Mech.*, **12**, 101–113.
- Lenn, Y.-D., and T. K. Chereskin, 2009: Observations of Ekman currents in the Southern Ocean. *J. Phys. Oceanogr.*, **39**, 768–779.
- , —, J. Sprintall, and E. Firing, 2007: Mean jets, mesoscale variability and eddy momentum fluxes in the surface-layer of the Antarctic Circumpolar Current. *J. Mar. Res.*, **65**, 27–58.
- Lewis, D. M., and S. E. Belcher, 2004: Time-dependent, coupled, Ekman boundary layer solutions incorporating Stokes drift. *Dyn. Atmos. Oceans*, **37**, 313–351.
- Madsen, O. S., 1977: A realistic model of the wind-induced Ekman boundary layer. *J. Phys. Oceanogr.*, **7**, 248–255.
- McWilliams, J. C., and J. M. Restrepo, 1999: The wave-driven ocean circulation. *J. Phys. Oceanogr.*, **29**, 2523–2540.
- , and E. Huckle, 2006: Ekman layer rectification. *J. Phys. Oceanogr.*, **36**, 1646–1659.
- , —, J.-H. Liang, and P. P. Sullivan, 2012: The wavy Ekman layer: Langmuir circulations, breaking waves, and Reynolds stress. *J. Phys. Oceanogr.*, **42**, 1793–1816.
- Polton, J. A., D. M. Lewis, and S. E. Belcher, 2005: The role of wave-induced Coriolis–Stokes forcing on the wind-driven mixed layer. *J. Phys. Oceanogr.*, **35**, 444–457.
- Price, J. F., and M. A. Sundermeyer, 1999: Stratified Ekman layers. *J. Geophys. Res.*, **104** (C9), 20 467–20 494.
- , R. A. Weller, and R. R. Schudlich, 1987: Wind-driven ocean currents and Ekman transport. *Science*, **238**, 1534–1538.
- Rudnick, D. L., P. Müller, and D. Henderson, Eds., 2003: Observations of momentum transfer in the upper ocean: Did Ekman get it right? *Near-Boundary Processes and Their Parameterization: Proc. 13th 'Aha Huliko 'a Hawaiian Winter Workshop*, Honolulu, HI, University of Hawai'i at Mānoa, 163–170.
- Smith, W. H. F., and D. T. Sandwell, 1997: Global sea floor topography from satellite altimetry and ship depth soundings. *Science*, **277**, 1956–1962, doi:10.1126/science.277.5334.1956.
- Sprintall, J., 2003: Seasonal to interannual upper-ocean variability in the Drake Passage. *J. Mar. Res.*, **61**, 25–57.
- Webb, A., and B. Fox-Kemper, 2011: Wave spectral moments and Stokes drift estimation. *Ocean Modell.*, **40**, 273–288, doi:10.1016/j.ocemod.2011.08.007.
- Wijffels, S., E. Firing, and H. Bryden, 1994: Direct observations of the Ekman balance at 10°N in the Pacific. *J. Phys. Oceanogr.*, **24**, 1666–1679.
- Yelland, M., and P. K. Taylor, 1996: Wind stress measurements from the open ocean. *J. Phys. Oceanogr.*, **26**, 541–558.
- Zikanov, O., D. N. Slinn, and M. R. Dhanak, 2003: Large-eddy simulations of the wind-induced turbulent Ekman layer. *J. Fluid Mech.*, **495**, 343–368.